IMA Journal of Applied Mathematics (2013) Page 1 of 17
doi:10.1093/imamat/hxt028

Long-wave equations and direct simulations for the breakup of a viscous fluid thread surrounded by an immiscible viscous fluid

M. R. Booty
Department of Mathematical Sciences and Center for Applied Mathematics and Statistics, New Jersey Institute of Technology, Newark, NJ 07102, USA
michael.r.booty@njit.edu

D. T. Papageorgiou*
Department of Mathematics, Imperial College, London SW7 2AZ, UK
*Corresponding author: d.papageorgiou@imperial.ac.uk

M. Siegel
Department of Mathematical Sciences and Center for Applied Mathematics and Statistics, New Jersey Institute of Technology, Newark, NJ 07102, USA
misieg@njit.edu

and

Q. Wang
Department of Mathematics, University of British Columbia, Vancouver, BC, Canada V6T 1Z4
qw6@njit.edu

[Received on 5 February 2013; revised on 25 March 2013; accepted on 25 March 2013]

We consider capillary driven breakup of a viscous liquid thread in a second immiscible viscous liquid of infinite extent and arbitrary viscosity. Postulating the existence of long-wave dynamics, we use the slenderness parameter $\epsilon \ll 1$ (proportional to the interfacial slope, for example) to construct consistent asymptotic theories using matched asymptotic expansions at arbitrary viscosity ratios. Three canonical models are found, two of which hold for asymptotically small values of the inner to outer viscosity ratio $\lambda \sim \epsilon^2$ and $\lambda \sim 1/\ln(1/\epsilon)$, respectively, and the third valid for large $\lambda \sim 1/(\epsilon^2 \ln(1/\epsilon))$. The smallest and largest λ produce appropriate limits of models described in the literature when the inner or outer fluid is air, respectively. The intermediate λ model is found to be ill-posed and a technique is described to regularize it by considering terms arising from the asymptotic forms of the $\lambda \sim \epsilon^2$ model as its scaled viscosity ratio becomes large, and from the asymptotic forms of the $\lambda \sim 1/(\epsilon^2 \ln(1/\epsilon))$ as its scaled viscosity becomes small. Time-dependent direct numerical simulations based on boundary integral methods are also used to predict the dynamics for a large range of viscosity ratios ($0.001 \leqslant \lambda \leqslant 20$). Intermediate values of λ indicate that the dynamics is not long-wave, consistent with the asymptotic analysis, but are self-similar in a pinch-off region with order one aspect ratio. Simulations at large and small values of λ produce intricate dynamics near pinching and in particular the formation of necks, threads and bulges. The direct simulations and the asymptotic models valid at $\lambda \sim \epsilon^2$ and $\lambda \sim 1/(\epsilon^2 \ln(1/\epsilon))$ complement each other and the former confirm the validity of the long-wave assumptions.

Keywords: interfacial flow; Stokes flow; asymptotic models; numerical simulation

1. Introduction

Liquid threads are encountered in numerous technological and industrial applications including ink-jet printing, extrusion processes and emulsification, spraying, electrospinning, to mention a few. The underlying phenomena are driven by capillary or Rayleigh instability—Rayleigh (1892)—that predicts that all waves longer than the undisturbed thread circumference are linearly unstable. Physically, a cylindrical liquid thread that supports surface tension tends to minimize its surface area by driving the system to drop formation. Utilizing this mechanism to produce a controlled stream of drops underpins established technologies such as ink-jet printing—for more recent microfluidics applications, see Anna *et al.* (2003). On the other hand, electric fields along the jet axis are used to suppress capillary instability as applied in electrospinning technologies. In addition to the temporal instability modes uncovered by Rayleigh, a liquid jet is also susceptible to spatial instabilities; these are disturbances with a fixed frequency of oscillation that can grow downstream as they travel, see Keller *et al.* (1973). As the Weber number (equivalently the undisturbed jet speed) is reduced below a critical value the jet exhibits absolute instability—two lower order poles in the dispersion relation merge to produce a pinch singularity—and the jet grows in both space and time. Such phenomena also appear when a jet is surrounded by a second fluid, as seen in the compound jet study of Chauhan *et al.* (2006). For an alternative analysis of absolute-convective instability for certain evolution PDEs, see Fokas & Papageorgiou (2005).

The present study is concerned with the non-linear dynamics and ultimate topological jet-pinching transitions that are seen in two-fluid jet systems, where a viscous liquid thread is surrounded by a second immiscible viscous liquid (taken to be unbounded in the radial direction). A combination of computational techniques has been applied by various authors and we mention the boundary integral computations for Stokes flows by Newhouse & Pozrikidis (1992), Pozrikidis (1999), Lister & Stone (1998) and Sierou & Lister (2003) along with Navier–Stokes computations by Chen *et al.* (2002), Hameed *et al.* (2008b) and Doshi *et al.* (2003). It is evident from all these theoretical studies as well as experiments (e.g. Cohen *et al.*, 1999; Kowalewski, 1996) that the presence of a surrounding viscous fluid influences significantly the analytical solutions found for single jets surrounded by a hydrodynamically passive medium—see Eggers & Dupont (1994) and Papageorgiou (1995).

The emergence of long-wave dynamics depends critically on the viscosity ratio; it has been shown that consistent long-wave models that can describe breakup can be found when the ratio of inner to outer fluid viscosity λ, say, is asymptotically small or large (see Doshi *et al.*, 2003; Lister & Stone, 1998, respectively). We employ rational asymptotic expansions to derive three canonical underlying long-wave models for $\lambda \sim \epsilon^2 \ll 1$, $\lambda \sim 1/\ln(1/\epsilon) \ll 1$ and $\lambda \sim 1/[\epsilon^2 \ln(1/\epsilon)] \gg 1$, where $\epsilon \ll 1$ denotes the slenderness ratio—see Section 2 for the definition. The $\lambda \ll 1$ models are characterized by a Poiseuille-like flow in the jet interior due to the viscous drag exerted by the surrounding fluid, whereas the latter scaling having $\lambda \gg 1$ induces a plug flow to leading order in the jet interior. This latter case corresponds to finite outer viscosity (albeit asymptotically small) modification of the equations studied by Papageorgiou (1995) and these are recovered in the appropriate limit. The asymptotic analysis is based on a combination of a long-wave lubrication approximation for the inner region fluid dynamics and these are matched to the outer unbounded domain flow at the interface. The outer flow is represented by an axially periodic distribution of singularities (Stokeslets and sources) placed on the jet axis; this follows the original ideas of Handelsman & Keller (1967) and Geer & Keller (1968) for potential flows and their extensions to Stokes flows by Buckmaster (1972) and Acrivos & Lo (1978). In addition to deriving long-wave models, we carry out direct simulations based on boundary integral methods using the techniques applied by Wang & Papageorgiou (2011) in a related problem. The computations follow capillary pinching for λ in the range $[0.001, 30]$; for λ neither too small nor too large (e.g. between 0.03 and 10, for instance), the breakup dynamics follow a self-similar scenario which is not long-wave,

in agreement with the findings of previous studies (e.g. Sierou & Lister, 2003). When λ is smaller or larger and hence outside this regime, more intricate behaviour is found including sequences of necks, threads and bulges in the vicinity of the pinch point. A full comparison between these simulations and the asymptotic models developed here will be carried out elsewhere.

2. Long-wave models for the breakup of a fluid thread

2.1 *Formulation*

Consider an infinitely long cylindrical thread of viscous fluid with viscosity $\lambda\mu$ surrounded by an immiscible, unbounded fluid with viscosity μ, so that λ is the ratio of the interior to exterior viscosity. We assume that inertia is sufficiently small for the evolution to be governed by the Stokes equations. The unperturbed radius of the fluid thread is b and constant surface tension σ acts at the interface.

We are interested in deriving consistent evolution equations valid for axisymmetric long-wave evolution of the thread that are capable of predicting pinching. See, for example, Papageorgiou (1995) for a successful application of such an asymptotic theory when $\lambda = \infty$. To achieve this, we assume that disturbances of the interface shape have a typical axial length scale of order l and the ratio $b/l = \epsilon \ll 1$. In a cylindrical polar coordinate system (r, θ, z), all lengths are non-dimensionalized by l, which leads to independent variables $\tilde{r} = r/\epsilon$ and z in the interior or thread region with r and z in the exterior region. With this scaling, axial perturbations are of order O(1) and the interface is located at $r = \epsilon\tilde{R}(z,t)$. Looking ahead, the separation of scales in the thread allows a lubrication analysis there, but the flow in the exterior region is governed by an elliptic problem whose solution is described later. Pressure is non-dimensionalized by the capillary pressure σ/b in the interior or thread region and by σ/l in the exterior region, while velocities, which are continuous across the interface that separates the two regions, are non-dimensionalized by the capillary velocity σ/μ, and time is non-dimensionalized by $\mu b/\sigma$. Dependent variables in the thread region are denoted by lower case letters and the corresponding quantities in the exterior region are denoted by upper case letters.

The governing equations are as follows:

In the interior or thread region, $0 < \tilde{r} < \tilde{R}(z,t)$

$$\lambda\left(\nabla_{\tilde{r}}^2 - \frac{1}{\tilde{r}^2} + \epsilon^2\frac{\partial^2}{\partial z^2}\right)u_r = \frac{\partial p}{\partial \tilde{r}}, \quad \frac{\lambda}{\epsilon}\left(\nabla_{\tilde{r}}^2 + \epsilon^2\frac{\partial^2}{\partial z^2}\right)u_z = \frac{\partial p}{\partial z}, \tag{2.1a}$$

$$\frac{1}{\tilde{r}}\frac{\partial}{\partial \tilde{r}}(\tilde{r}u_r) + \epsilon\frac{\partial u_z}{\partial z} = 0. \tag{2.1b}$$

In the exterior region, $r > \epsilon\tilde{R}(z,t)$

$$\left(\nabla_r^2 - \frac{1}{r^2} + \frac{\partial^2}{\partial z^2}\right)U_r = \frac{\partial P}{\partial r}, \quad \left(\nabla_r^2 + \frac{\partial^2}{\partial z^2}\right)U_z = \frac{\partial P}{\partial z}, \tag{2.2a}$$

$$\frac{1}{r}\frac{\partial}{\partial r}(rU_r) + \frac{\partial U_z}{\partial z} + = 0. \tag{2.2b}$$

Here, $\nabla_r^2 = (1/r)(\partial/\partial r)(r(\partial/\partial r))$ and a similar expression for $\nabla_{\tilde{r}}^2$ represent the radial derivatives of the Laplacian.

The boundary conditions on the thread axis are

$$u_r(0,z,t) = \frac{\partial u_z}{\partial \tilde{r}}(0,z,t) = 0, \tag{2.3}$$

and in the exterior region

$$U_r, U_z \to 0 \quad \text{as } r \to \infty. \tag{2.4}$$

At the interface $r = \epsilon\tilde{R}(z,t)$, the conditions to be satisfied are continuity of velocity, the kinematic condition and continuity of stress. The length scale for non-dimensionalization of these is l, and below we use primes to denote $\partial/\partial z$:

Continuity of velocity

$$u_r = U_r, \quad u_z = U_z. \tag{2.5}$$

The kinematic condition

$$\tilde{R}_t - u_r + \epsilon u_z \tilde{R}' = 0. \tag{2.6}$$

Tangential stress balance

$$\begin{aligned}\lambda\left\{\tilde{R}'\frac{\partial u_r}{\partial \tilde{r}} + \frac{1}{2}(1-\epsilon^2\tilde{R}'^2)\left(\frac{\partial u_r}{\partial z} + \frac{1}{\epsilon}\frac{\partial u_z}{\partial \tilde{r}}\right) - \epsilon\tilde{R}'\frac{\partial u_z}{\partial z}\right\} \\ = \left\{\epsilon\tilde{R}'\frac{\partial U_r}{\partial r} + \frac{1}{2}(1-\epsilon^2\tilde{R}'^2)\left(\frac{\partial U_r}{\partial z} + \frac{\partial U_z}{\partial r}\right) - \epsilon\tilde{R}'\frac{\partial U_z}{\partial z}\right\}.\end{aligned} \tag{2.7}$$

Normal stress balance

$$\begin{aligned}p - \frac{2\epsilon\lambda}{(1+\epsilon^2\tilde{R}'^2)}\left\{\frac{1}{\epsilon}\frac{\partial u_r}{\partial \tilde{r}} - \epsilon\tilde{R}'\left(\frac{\partial u_r}{\partial z} + \frac{1}{\epsilon}\frac{\partial u_z}{\partial \tilde{r}}\right) + \epsilon^2\tilde{R}'^2\frac{\partial u_z}{\partial z}\right\} \\ - \epsilon P + \frac{2\epsilon}{(1+\epsilon^2\tilde{R}'^2)}\left\{\frac{\partial U_r}{\partial r} - \epsilon\tilde{R}'\left(\frac{\partial U_r}{\partial z} + \frac{\partial U_z}{\partial r}\right) + \epsilon^2\tilde{R}'^2\frac{\partial U_z}{\partial z}\right\} \\ = \frac{1}{\tilde{R}(1+\epsilon^2\tilde{R}'^2)^{1/2}}\left\{1 - \frac{\epsilon^2\tilde{R}\tilde{R}''}{(1+\epsilon^2\tilde{R}'^2)}\right\}.\end{aligned} \tag{2.8}$$

Here, all quantities are evaluated on the interface, so that with our choice of radial coordinates, dependent variables and their derivatives in the interior or thread region (denoted in lower case) are evaluated on $\tilde{r} = \tilde{R}(z,t)$, while analogous quantities in the exterior region (upper case) are evaluated on $r = \epsilon\tilde{R}(z,t)$.

Our interest is to construct asymptotic long-wave models in the limit in which the fluid of the interior region is a small aspect ratio 'thread', that is, as $\epsilon \to 0$ with the interface slope $\tilde{R}'(z,t)$ of order O(1).

2.2 *The solution in the exterior or surrounding fluid*

The assumption of small aspect ratio implies that flow quantities in the exterior fluid can be expressed in terms of a distribution of point forces or Stokeslets $f(z,t)$, that act in the axial direction, and a distribution of point mass sources $g(z,t)$, where both distributions are located on the thread axis $r = 0$. The evaluation of flow quantities on the interface is given in the classical results of slender body theory for Stokes flow, of which two early examples are Buckmaster (1972) and Acrivos & Lo (1978). The

expressions that result and more details of their derivation are given in, for example, Hameed *et al.* (2008a).

To summarize, in terms of f and g the flow quantities and their derivatives in the exterior fluid, evaluated at the interface $r = \epsilon\tilde{R}(z,t)$, are given by

$$U_r = -2\epsilon \ln(1/\epsilon) f' \tilde{R} + \frac{2g}{\epsilon\tilde{R}} + \cdots, \quad U_z = 4\ln(1/\epsilon) f - 2\ln(1/\epsilon) g' + \cdots, \tag{2.9a}$$

$$P = -4\ln(1/\epsilon) f' + \cdots, \quad \frac{\partial U_r}{\partial r} = -2\ln(1/\epsilon) f' - \frac{2g}{\epsilon^2\tilde{R}^2} + \cdots, \tag{2.9b}$$

$$\frac{\partial U_r}{\partial z} + \frac{\partial U_z}{\partial r} = -\frac{4f}{\epsilon\tilde{R}} + \frac{4g'}{\epsilon\tilde{R}} + \cdots, \quad \frac{\partial U_z}{\partial z} = 4\ln(1/\epsilon) f' - 2\ln(1/\epsilon) g'' + \cdots. \tag{2.9c}$$

Here and below, an ellipsis denotes terms that are of higher order. The distributions f and g that appear in these expressions have not yet been scaled with respect to ϵ. Scalings are sought below, by looking for distinguished limits that relate the viscosity ratio λ to ϵ in different regimes as $\epsilon \to 0$, and which result from satisfying the interfacial boundary conditions (2.5–2.8).

2.3 *The solution in the interior fluid*

A crucial observation that allows a rational determination of the different scaling relations between λ and ϵ is that the flow induced in the interior fluid has a velocity profile that is either of Poiseuille- or plug-flow type.

To see that these are the only two allowable forms of velocity profile within the thread, we introduce a stream function ψ, where $u_r = (-\epsilon/\tilde{r})(\partial\psi/\partial z)$ and $u_z = (1/\tilde{r})(\partial\psi/\partial\tilde{r})$. Eliminating the pressure p between (2.1a), we find that ψ satisfies

$$\left\{\tilde{r}\frac{\partial}{\partial\tilde{r}}\nabla_{\tilde{r}}^2\left(\frac{1}{\tilde{r}}\frac{\partial}{\partial\tilde{r}}\right) + \epsilon^2\frac{\partial^2}{\partial z^2}\left(\tilde{r}\frac{\partial}{\partial\tilde{r}}\left(\frac{1}{\tilde{r}}\frac{\partial}{\partial\tilde{r}}\right)\right) + \tilde{r}\left(\nabla_{\tilde{r}}^2 - \frac{1}{\tilde{r}^2}\right)\frac{1}{\tilde{r}}\right) + \epsilon^4\frac{\partial^4}{\partial z^4}\right\}\psi = 0. \tag{2.10}$$

So that, to leading order, from the boundary conditions (2.3) the stream function is given by

$$\psi_0 = A_0(z,t)\frac{\tilde{r}^4}{16} + B_0(z,t)\frac{\tilde{r}^2}{2}. \tag{2.11}$$

Using the stream function (2.11) to reconstruct the velocity and pressure, and then rescaling so that the pressure p inside the thread is O(1), when $A_0 = \partial p_0/\partial z \neq 0$ we find a Poiseuille-type velocity profile

$$\begin{aligned} p &= p_0(z,t) + \cdots, \quad u_z = \frac{\epsilon}{\lambda}\left(\frac{\partial p_0}{\partial z}\frac{\tilde{r}^2}{4} + B_0(z,t)\right) + \cdots, \\ u_r &= \frac{-\epsilon^2}{\lambda}\left(\frac{\partial^2 p_0}{\partial z^2}\frac{\tilde{r}^3}{16} + \frac{\partial B_0}{\partial z}(z,t)\frac{\tilde{r}}{2}\right) + \cdots. \end{aligned} \tag{2.12}$$

However, when $A_0 = 0$ we find a plug-type velocity profile

$$p = p_0(z,t) + \cdots, \quad u_z = \frac{1}{\epsilon\lambda}B_0(z,t) + \cdots, \quad u_r = \frac{-1}{\lambda}\frac{\partial B_0}{\partial z}(z,t)\frac{\tilde{r}}{2} + \cdots. \tag{2.13}$$

To estimate the order of magnitude of the component of the velocity gradient $\partial u_z/\partial\tilde{r}$ for plug flow, we return to the axial component of the momentum equation (2.1a) to find that radial dependence of u_z

occurs at an order ϵ^2 smaller than leading order, and that

$$u_z = \frac{1}{\epsilon\lambda}B_0(z,t) + \cdots + \frac{\epsilon}{\lambda}\left(\left(\frac{\partial p_0}{\partial z} - \frac{\partial^2 B_0}{\partial z^2}\right)\frac{\tilde{r}^2}{4} + B_1(z,t)\right) + \cdots . \tag{2.14}$$

2.3.1 *Poiseuille flow in the interior fluid* We perform order of magnitude estimates on the interfacial boundary conditions when the flow in the thread is of Poiseuille type, per (2.12). We then look for scalings of λ, f and g with respect to ϵ that provide a leading-order balance between a maximal number of terms in each of the interfacial boundary conditions.

Continuity of radial velocity at the interface per (2.5), with (2.9a) and (2.12), gives

$$\frac{-\epsilon^2}{\lambda}\left(\frac{\partial^2 p_0}{\partial z^2}\frac{\tilde{R}^3}{16} + \frac{\partial B_0}{\partial z}\frac{\tilde{R}}{2}\right) = -2\epsilon\ln(1/\epsilon)f'\tilde{R} + \frac{2g}{\epsilon\tilde{R}}. \tag{2.15}$$

On multiplying through by λ/ϵ^2, we have a potential balance between terms of orders O(1), O($(\lambda\ln(1/\epsilon)/\epsilon)f'$) and O($(\lambda/\epsilon^3)g$). Continuity of axial velocity at the interface, per (2.5) with (2.9a) and (2.12), gives

$$\frac{\epsilon}{\lambda}\left(\frac{\partial p_0}{\partial z}\frac{\tilde{R}^2}{4} + B_0\right) = 4\ln(1/\epsilon)f. \tag{2.16}$$

Here, the term in g' of (2.9a) has been neglected since its magnitude relative to the term in f is necessarily smaller than that given by a leading-order balance in (2.15). On multiplying through by λ/ϵ, (2.16) gives a potential balance between terms of order O(1) and O($(\lambda\ln(1/\epsilon)/\epsilon)f$), so that no further information for the scalings, relative to that already given by (2.15), is found.

Of the conditions to be satisfied at the interface, the kinematic condition (2.6) is the only one that contains a time derivative, and it may be necessary to introduce a new time scale $\tau = \delta t$ in order to retain a time derivative in the evolution equation that is sought for the interface position $\tilde{R}$. From the continuity of velocity at the interface, the velocity components can be expressed in terms of the Stokeslet and mass source distributions f and g, respectively, so that (2.6) with (2.9a) gives

$$\delta\tilde{R}_\tau = \epsilon\ln(1/\epsilon)\left(-2f'\tilde{R} - 4f\tilde{R}'\right) + \frac{2g}{\epsilon\tilde{R}}. \tag{2.17}$$

As in (2.16), the term in g' that appears in the axial velocity of (2.9a) has been omitted here since it is of higher order. The terms in (2.17) are of order O(δ), O($\epsilon\ln(1/\epsilon)f$) and O(g/ϵ), and we note that the ratio of the magnitude of the terms containing f and g is the same as that found in (2.15), so that for the scalings sought, only information about δ is provided by a balance of terms in (2.17).

In the tangential stress balance condition at the interface (2.7), when the interior flow is of Poiseuille type from (2.12) the one component $\partial u_z/\partial\tilde{r}$ of the velocity gradient provides a contribution that is of greater magnitude than all others to the tangential stress in the interior fluid. With (2.9b) and (2.9c), the tangential stress balance gives a potential leading-order balance among terms of the equation

$$\frac{\partial p_0}{\partial z}\frac{\tilde{R}}{4} = -\frac{2f}{\epsilon\tilde{R}} - \frac{2g\tilde{R}'}{\epsilon\tilde{R}^2} + \frac{2g'}{\epsilon\tilde{R}}. \tag{2.18}$$

These are of magnitudes O(1), O(f/ϵ) and O(g/ϵ).

In the normal stress balance condition (2.8), contributions to the viscous stress due to the interior fluid are estimated from (2.12) and found to be at most of order $O(\epsilon^2)$, and are therefore neglected relative to the interior pressure and surface tension, which are O(1). Contributions to the normal stress due to the exterior fluid are estimated from (2.9b) and (2.9c). The term of greatest magnitude that contains f is of order $O(\epsilon \ln(1/\epsilon) f')$, which by comparison with (2.18) is necessarily of higher-order relative to the interior pressure and surface tension. The Stokeslet distribution f therefore does not appear in the leading-order normal stress balance, which becomes

$$p_0 - \frac{4g}{\epsilon \tilde{R}^2} = \frac{1}{\tilde{R}}. \tag{2.19}$$

These are of magnitude O(1) and $O(g/\epsilon)$, which are in the same ratio as found in the tangential stress balance relation (2.18), so that no further information for the scaling of g is found.

To find scalings that balance a maximal number of terms, we therefore have the information provided by continuity of radial velocity at (2.15) and the tangential stress balance at (2.18) alone. Continuity of radial velocity implies a possible balance of terms among

$$1, \quad \lambda \frac{\ln(1/\epsilon)}{\epsilon} f' \quad \text{and} \quad \lambda \frac{g}{\epsilon^3}, \tag{2.20}$$

and the tangential stress balance implies a possible balance among

$$1, \quad \frac{f}{\epsilon} \quad \text{and} \quad \frac{g}{\epsilon}. \tag{2.21}$$

The kinematic condition then gives the magnitude of the time scale δ, from a balance of terms among

$$\delta, \quad \epsilon \ln(1/\epsilon) f \quad \text{and} \quad \frac{g}{\epsilon}. \tag{2.22}$$

We note that the ratio of terms containing f and g is the same in both (2.20) and (2.22).

By inspection, not all terms of (2.20) and (2.21) can enter a balance, and there are two consistent choices or canonical regimes for λ as follows:

1. $f \sim \epsilon$ and $g \sim \epsilon$ to balance all terms in (2.21); then $\lambda \sim \epsilon^2$ for a consistent balance in (2.20). In this case, (2.16) implies that the axial velocity $u_z(\tilde{R}, z, t) = 0$ on the interface and (2.22) implies that $\delta = 1$;
2. $g \sim \epsilon^2 \ln(1/\epsilon) f'$ and $\lambda \sim \epsilon^3 / g$ to balance all terms in (2.20); then $f \sim \epsilon$ for a consistent balance in (2.21). This gives $g \sim \epsilon^3 \ln(1/\epsilon)$ and $\lambda \sim 1/\ln(1/\epsilon)$, with $\delta \sim \epsilon^2 \ln(1/\epsilon)$.

The scaling $\lambda \sim \epsilon^2$ at 1 has been considered by Doshi *et al.* (2003) and Sierou & Lister (2003). For completeness, we include some details of the derivation of the long-wave model for this scaling regime in the Appendix, but the result is needed in the discussion below. Putting $\lambda = \epsilon^2 \lambda_0$, where $\lambda_0 = O(1)$, dropping the zero-subscript on p_0 and writing R for $\tilde{R}$ (with some overuse of notation), we have

$$\frac{\partial R}{\partial \tau} = \frac{1}{16 \lambda_0} \frac{1}{R} \frac{\partial}{\partial z} \left(R^4 \frac{\partial p}{\partial z} \right), \tag{2.23}$$

$$p = \frac{1}{R} + \frac{2}{R} \frac{\partial R}{\partial \tau}. \tag{2.24}$$

Together with initial and boundary conditions this forms a closed system for the determination of R and p.

We proceed with the scaling at 2 above, and write

$$\lambda = \frac{\lambda_1}{\ln(1/\epsilon)}, \quad f = \epsilon f_0 + \cdots, \quad g = \epsilon^3 \ln(1/\epsilon) g_0 + \cdots, \quad \delta = \epsilon^2 \ln(1/\epsilon), \tag{2.25a}$$

$$u_z = \epsilon \ln(1/\epsilon) u_{z0} + \cdots, \quad u_r = \epsilon^2 \ln(1/\epsilon) u_{r0} + \cdots, \quad p = p_0 + \cdots, \quad \tilde{R} = R_0 + \cdots. \tag{2.25b}$$

This scaling retains all terms among (2.20), and hence all leading terms among (2.15–2.17), which become

$$\frac{1}{\lambda_1}\left(\frac{\partial^2 p_0}{\partial z^2}\frac{R_0^3}{16} + \frac{\partial B_0}{\partial z}\frac{R_0}{2}\right) = 2_0 f_0' R_0 - \frac{2g_0}{R_0}, \quad u_r \text{ continuous}, \tag{2.26}$$

$$\frac{1}{\lambda_1}\left(\frac{\partial p_0}{\partial z}\frac{R_0^2}{4} + B_0\right) = 4f_0, \quad u_z \text{ continuous}, \tag{2.27}$$

$$\partial_\tau R_0 = -2f_0' R_0 - 4f_0 R_0' + \frac{2g_0}{R_0}, \quad \text{kinematic condition}. \tag{2.28}$$

In the stress-balance boundary condition, the mass source distribution g does not contribute at leading order in this scaling regime, and after a little rearrangement we have

$$f_0 = -\frac{R_0^2}{8}\frac{\partial p_0}{\partial z}, \quad \text{tangential stress balance}, \tag{2.29}$$

$$p_0 = \frac{1}{R_0}, \quad \text{normal stress balance}. \tag{2.30}$$

Both B_0 and f_0 can be eliminated between (2.26) and (2.27) to give an expression for the mass source strength g_0, while (2.28) gives f_0 directly. Both expressions are in terms of R_0 and p_0. Then, from (2.28) and (2.30), after dropping zero-subscripts, we find the pair of long-wave evolution equations

$$\frac{\partial R}{\partial \tau} = \left(\frac{1}{4} + \frac{1}{16\lambda_1}\right)\frac{1}{R}\frac{\partial}{\partial z}\left(R^4\frac{\partial p}{\partial z}\right), \tag{2.31}$$

$$p = \frac{1}{R}. \tag{2.32}$$

From (2.27) and (2.29), the term B_0 that appears in the velocity profile (2.12) is given by $B_0 = -(1 + 2\lambda_1)(R^2 p'/4)$.

2.3.2 *Plug flow in the interior fluid.* When the flow in the thread is of the plug-flow type, the velocity profile is given by (2.13). Long-wave models for this case have been considered by Papageorgiou (1995) for a Stokes flow thread and by Eggers & Dupont (1994) for a Navier–Stokes thread, with inviscid surroundings adopted in both studies. Lister & Stone (1998) extended the long-wave model for a Stokes flow thread to include viscous surroundings, by somewhat heuristic reasoning, and the result is given here.

There is only one significant scaling regime when the flow in the thread is of the plug-flow type, and the scalings are

$$\lambda = \frac{\lambda_2}{\epsilon^2 \ln(1/\epsilon)}, \quad f = \epsilon f_0 + \cdots, \quad g = o(\epsilon^3 \ln(1/\epsilon)), \quad \delta = \epsilon^2 \ln(1/\epsilon), \tag{2.33a}$$

$$u_z = \epsilon \ln(1/\epsilon) u_{z0} + \cdots, \quad u_r = \epsilon^2 \ln(1/\epsilon) u_{r0} + \cdots, \quad p = p_0 + \cdots, \quad \tilde{R} = R_0 + \cdots. \tag{2.33b}$$

The long-wave model is given by

$$\frac{\partial R}{\partial \tau} + w \frac{\partial R}{\partial z} + \frac{R}{2} \frac{\partial w}{\partial z} = 0, \tag{2.34}$$

$$\lambda_2 \frac{\partial}{\partial z} \left(3R^2 \frac{\partial w}{\partial z} \right) + \frac{\partial R}{\partial z} = 2w, \tag{2.35}$$

where the zero-subscript on R_0 has been dropped and we have set $u_{z0} = w$.

3. Discussion of the long-wave models

The three long-wave models given above agree or match when the relevant limits of the viscosity ratio are formed.

To see this, first consider the limit of the small viscosity regime model (2.23) and (2.24) as its viscosity parameter $\lambda_0 \to \infty$. Since $\delta = 1$ in this regime, per (A.1a), it has time $\tau = t$. If this is rescaled to a new time $\bar{\tau} = \tau/\lambda_0$ and the limit $\lambda_0 \to \infty$ is taken, after eliminating p, one finds the single equation

$$\frac{\partial R}{\partial \bar{\tau}} = \frac{1}{16R} \frac{\partial}{\partial z} \left(R^4 \frac{\partial}{\partial z} \left(\frac{1}{R} \right) \right), \tag{3.1}$$

for R, where $\bar{\tau}$ is a slow time relative to $\tau = t$. This is the same as the limit of the intermediate viscosity regime model of (2.31) and (2.32) when its viscosity parameter $\lambda_1 \to 0$. To form this limit, the slow time τ of (2.31) is rescaled to $\bar{\tau} = \tau/\lambda_1$ and p is eliminated via (2.32). In this case, $\bar{\tau}$ is a fast time relative to the time τ of (2.31) and (2.32).

Next, consider the limit of the intermediate viscosity regime model of (2.31) and (2.32) when its viscosity parameter $\lambda_1 \to \infty$. Eliminating p between (2.31) and (2.32), we immediately find the equation

$$\frac{\partial R}{\partial \tau} = \frac{1}{4R} \frac{\partial}{\partial z} \left(R^4 \frac{\partial}{\partial z} \left(\frac{1}{R} \right) \right), \tag{3.2}$$

which is also (3.1) with time rescaled. Equation (3.2) is the same as the limit of the large viscosity regime model (2.34) and (2.35) as its viscosity parameter $\lambda_2 \to 0$, as is seen once w is eliminated and a little manipulation of the z-derivatives is performed.

3.1 *The leading-order intermediate viscosity regime model is ill-posed*

It turns out that the intermediate viscosity regime model of (2.31) and (2.32) is ill-posed in the sense that the growth rate of small-amplitude disturbances of a cylindrical thread grow without bound with decreasing wavelength (on the other hand, note that the small and large λ models are linearly well-posed in the sense that disturbances do not have unbounded growth rates as the wavenumber tends to infinity).

On setting $R = 1 + \xi(z,t)$ in (2.31) and (2.32) and linearizing, we find the backward heat equation

$$\xi_\tau = -\frac{1}{4}\left(1 + \frac{1}{4\lambda_1}\right)\xi_{zz}. \tag{3.3}$$

It follows immediately that the large viscosity limit of the small viscosity model, given by (3.1), and the small viscosity limit of the large viscosity model, given by (3.2), are also ill-posed, since both are found when p is eliminated between (2.31) and (2.32) and time is rescaled.

3.2 *Regularization*

Both of the limiting evolution equations (3.1) and (3.2) hold at leading order. The inclusion of viscous effects in either of the models (2.23–2.24) or (2.34–2.35) at the next order can render them well-posed or, in other words, regularize them.

Consider the small viscosity model (2.23–2.24) first. To form a regularized model when $\lambda_0 \gg 1$, it is necessary to use (2.23) to express the time derivative $\partial_\tau R$ in (2.24) in terms of spatial derivatives, and then to rescale to the new time $\bar{\tau} = \tau/\lambda_0$ that was introduced in (3.1). Put $p = R^{-1} + Q/\lambda_0 + \cdots$ to find an expression in terms of spatial derivatives for Q. On substitution of this in the time-rescaled version of (2.23), one finds

$$\frac{\partial R}{\partial \bar{\tau}} = \frac{1}{16R}\frac{\partial}{\partial z}\left(R^4\frac{\partial}{\partial z}\left(\frac{1}{R}\right)\right) + \frac{1}{128\lambda_0 R}\frac{\partial}{\partial z}\left(R^4\frac{\partial}{\partial z}\left(\frac{1}{R^2}\frac{\partial}{\partial z}\left(R^4\frac{\partial}{\partial z}\left(\frac{1}{R}\right)\right)\right)\right). \tag{3.4}$$

Small-amplitude, linearized disturbances given by $R = 1 + \xi(z,t)$ satisfy

$$\xi_{\bar{\tau}} = -\frac{1}{16}\xi_{zz} - \frac{1}{128\lambda_0}\xi_{zzzz}. \tag{3.5}$$

The fourth derivative term regularizes the model equation by damping the growth of short wavelength disturbances. It has the same eigenvalues as the linearized Kuramoto–Sivashinsky equation; see, for example, the review by Hyman & Nicolaenko (1986).

To regularize the large viscosity model (2.34–2.35) when $\lambda_2 \ll 1$, put $w = (\partial_z R/2) + \lambda_2\tilde{Q} + \cdots$ in (2.35) to find that $\tilde{Q} = \frac{3}{4}\partial_z(R^2\partial_z^2 R)$. Then, from (2.34) we have

$$\frac{\partial R}{\partial \tau} = \frac{1}{4R}\frac{\partial}{\partial z}\left(R^4\frac{\partial}{\partial z}\left(\frac{1}{R}\right)\right) - \frac{3\lambda_2}{8R}\frac{\partial}{\partial z}\left(R^2\frac{\partial}{\partial z}\left(R^2\frac{\partial^2 R}{\partial z^2}\right)\right). \tag{3.6}$$

Linearized small-amplitude disturbances $\xi(z,t)$, where $R = 1 + \xi(z,t)$, satisfy

$$\xi_\tau = -\frac{1}{4}\xi_{zz} - \frac{3\lambda_2}{8}\xi_{zzzz}, \tag{3.7}$$

and, as at (3.5), the fourth derivative term regularizes the model.

A means of regularizing the intermediate viscosity model is to include higher-order terms in ϵ in the curvature or capillary stress term of the normal stress-balance boundary condition (2.8). In a long-wave approximation, the leading-order effect of curvature is given by the component in the plane $z =$ constant, which is sometimes referred to as hoop stress. The component in the orthogonal plane adds a higher-order z-derivative to the second of (2.31) and (2.32), to give $p = 1/R - \epsilon^2\partial_z^2 R$. Linearized

small-amplitude disturbances $\xi(z,t)$, where $R = 1 + \xi(z,t)$, then satisfy

$$\xi_\tau = -\frac{1}{4}\left(1 + \frac{1}{4\lambda_1}\right)\left(\xi_{zz} + \epsilon^2 \xi_{zzzz}\right), \tag{3.8}$$

which provides a high frequency cut-off or negative growth rate for disturbances with wavelength less than $O(\epsilon)$.

4. Direct numerical simulations

In this section, we report on numerical simulations for the capillary breakup of a slender drop in Stokes flow. The velocity on the drop interface is governed by the boundary integral equation (see Lister & Stone, 1998 or Pozrikidis, 1999)

$$u_\alpha(\mathbf{x}_0) - \frac{\lambda - 1}{4\pi(\lambda + 1)} \int_I^{PV} Q_{\alpha\beta\gamma}(\mathbf{x}, \mathbf{x}_0) u_\beta(\mathbf{x}) n_\gamma(\mathbf{x})\, \mathrm{d}l(\mathbf{x})$$
$$= -\frac{1}{4\pi(\lambda + 1)} \int_I \kappa M_{\alpha\beta}(\mathbf{x}, \mathbf{x}_0) n_\beta(\mathbf{x})\, \mathrm{d}l(\mathbf{x}), \tag{4.1}$$

where I is the interface profile, which has outward normal $\boldsymbol{n}$ and curvature κ. Here $Q_{\alpha\beta\gamma}$ and $M_{\alpha\beta}$ are the axisymmetric version of the Stresslet distribution (or double layer potential) and the Stokeslet distribution (or single layer potential), respectively. An adaptive grid technique, which is similar to that described by Lister & Stone (1998), is used to resolve the necking region before pinch-off. In the computations reported here, the initial interface profile was represented by about 200 points, which was increased to around 450 at the time of the final profile. In addition to axisymmetry, the interface is symmetric about the plane $z = 0$. The initial interface profile is sufficiently elongated that, near the point where the drop pinches of,f the dynamics is expected to closely follow the dynamics of an axially periodic thread.

Our interest is in the behaviour near pinch-off as the viscosity ratio λ varies. This has been considered theoretically by Zhang & Lister (1999) and Sierou & Lister (2003), and in experiments by Cohen *et al.* (1999) and Kowalewski (1996). To compare with the majority of these studies, in this section the thread radius is denoted by h instead of R, the axial fluid velocity is v and the radial velocity is u, instead of u_z and u_r, respectively.

Lister & Stone (1998) use scaling arguments in the intermediate to large viscosity regime to reason that both the minimum radius of a thread $h_{\min}$ and the axial scale near the pinch point $z_{\min} = z(h_{\min})$ behave linearly in time as pinch-off is approached. They support this with the results of boundary integral computations when $\lambda = 1$, and we show the results of our computations at the same viscosity ratio in Fig. 1. Figure 1(a) shows the interface profile from the initial instant to a time $\tau = (t_s - t)$ of approximately 10^{-3} just before pinch-off, when the minimum thread radius is close to 10^{-4}; here t_s denotes our numerical estimate of the pinch-off time. Figure 1(b) shows the axial velocity versus z at the same sequence of times. Figure 1(c) shows the minimum thread radius $h_{\min}$ versus τ in a log–log plot, which confirms the scaling relation $h_{\min} \sim \tau$; the dashed line has slope 1. Figure 1(d) shows the axial velocity $v_{h_{\min}}$ at the minimum thread radius versus the logarithm of the minimum thread radius $\ln(h_{\min})$. This shows a logarithmic increase in $v_{h_{\min}}$, and the slope of the dashed line in this panel is in complete agreement with the results of Lister & Stone (1998), which they put on a sound theoretical footing based on the asymptotic behaviour of the thread profile away from the pinch point towards a pair of cones.

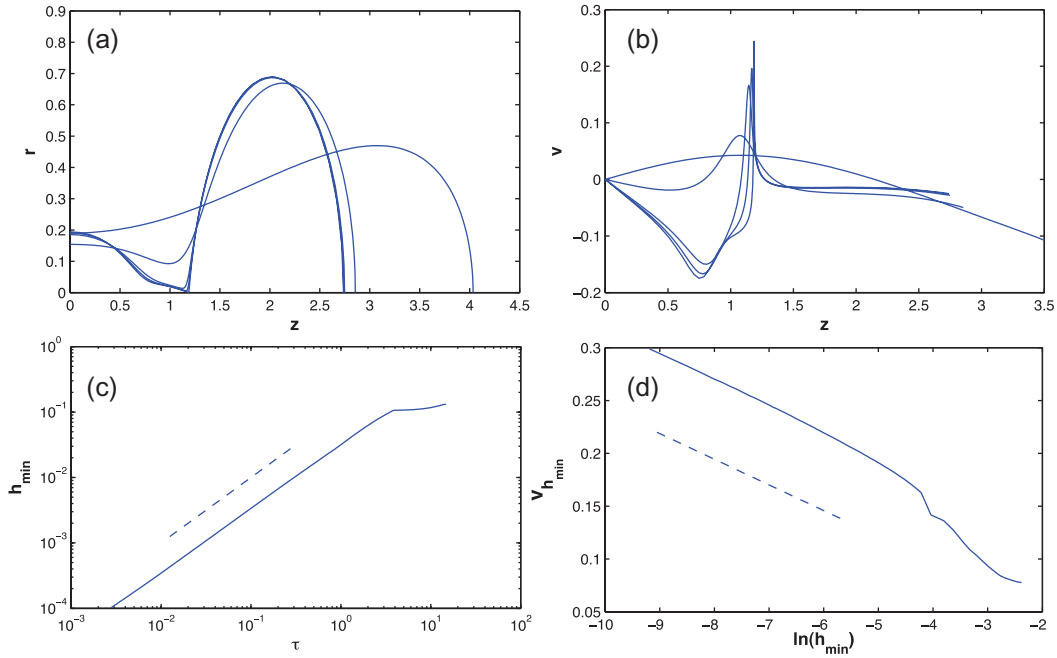

FIG. 1. Evolution of a drop with viscosity ratio $\lambda = 1$ approaching pinch-off. (a) Interface profiles at a sequence of times as time to pinch-off $\tau \to 0$. (b) Axial velocity v on the interface versus axial coordinate z at the same sequence of times. (c) The log–log plot of minimum radius $h_{\min}$ versus τ. (d) Axial velocity $v_{h_{\min}}$ at the minimum radius $z = h_{\min}$ versus $\ln(h_{\min})$, with the slope of dashed line showing that $v_{h_{\min}} \sim -0.0243 \ln(h_{\min}) + \text{constant}$.

Following these earlier studies, we introduce the similarity variables

$$\xi = \frac{z - z_{\min}}{h_{\min}}, \quad H(\xi) = \frac{h}{h_{\min}}. \tag{4.2}$$

By expressing profile data at times close to pinch-off in terms of $H(\xi)$ and ξ, our computations support the conclusion that in a neighbourhood of the pinch point the profile takes a self-similar form when λ is in the approximate range $0.02 < \lambda < 20$, as seen in the top three panels of Figure 2.

For very small and very large values of λ, the approach to self-similar structure, if it occurs, is less clear. The lower panels of Fig. 2 show results of simulations when $\lambda = 0.001$ (left panel) and $\lambda = 30$ (right panel) over a larger interval in ξ. In both cases, oscillations of the rescaled profile appear away from $\xi = 0$. This is consistent with the emergence of fine-scale structure of the thread profile that develops as pinch-off is approached, which appears to be more prevalent at more extreme values of λ. Two examples of fine-scale structure are shown in Fig. 3 when $\lambda = 0.02$ (top panels) and $\lambda = 30$ (lower panels). These show typical thread structures that occur at these values of λ although they have developed from different initial thread profiles from the data of Figs 1 and 2. The right-hand panels show that on increasingly small length scales as pinch-off is approached, a sequence of necks, threads and bulges form, and the location $z_{\min}$ of the minimum thread radius can change discontinuously when the decrease in radius at a minimum is overtaken by the decrease at a location nearby. This behaviour has been noted in many numerical simulations of capillary pinch-off and in the experiments reported,

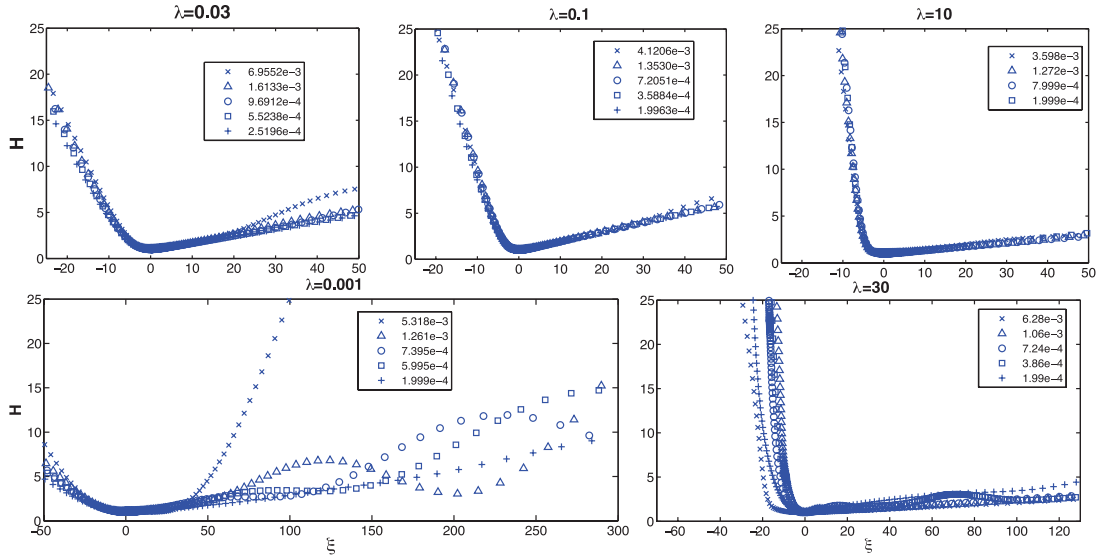

FIG. 2. Rescaled profiles showing $H(\xi) = h/h_{\min}$ versus $\xi = (z - z_{\min})/h_{\min}$ for different λ. $\lambda = 0.03$, 0.1 and 10 show a collapse of the data to self-similar form as pinch-off approaches, while sufficiently small or large λ do not show such collapse convincingly, if it occurs. The legend indicates values of minimum neck radius $h_{\min}$ for which the data are extracted from the time-dependent computations.

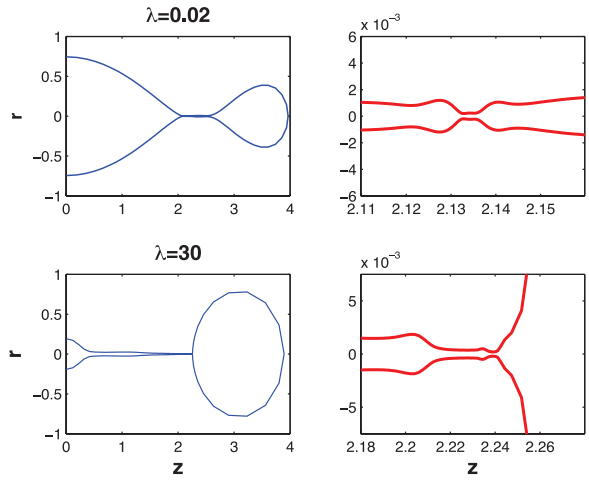

FIG. 3. Interface profiles near pinch-off with $\lambda = 0.02$ (upper panels) and $\lambda = 30$ (lower panels). The left-hand panels show the global interface shape and the right-hand panels show fine-scale structure in a close-up near the pinch point.

for example, by Cohen *et al.* (1999) and Kowalewski (1996). Brenner *et al.* (1996) develop stability results for families of similarity solutions that occur in long-wave models of pinch-off which may offer a theoretical basis for this.

Figure 4 shows self-similar profiles extracted from the data at the final time just before pinch-off for λ in the range $0.03 \leqslant \lambda \leqslant 1$ in Fig. 4(a) and in the range $1 \leqslant \lambda \leqslant 20$ in Fig. 4(b). The profiles closely

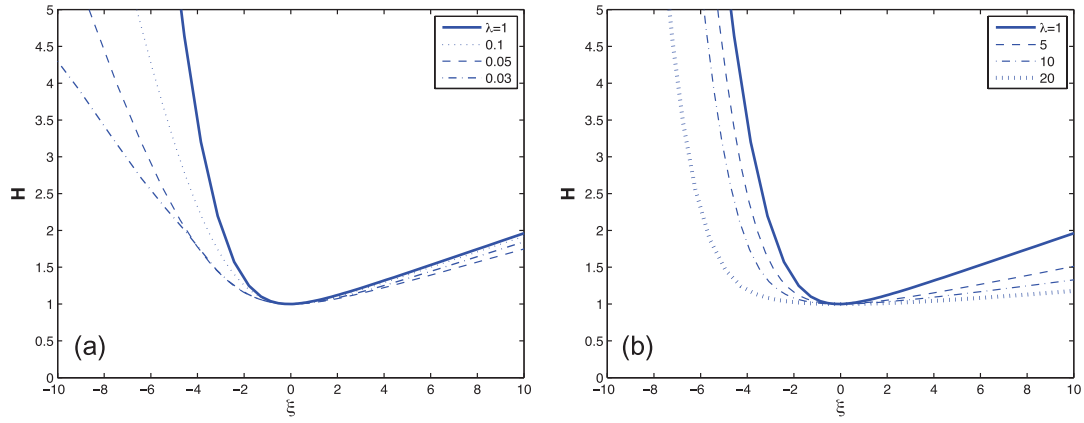

FIG. 4. Self-similar profiles extracted from the data near pinch-off, with $\lambda = 0.03$, 0.05, 0.1 and 1 in (a) and $\lambda = 1$, 5, 10 and 20 in (b).

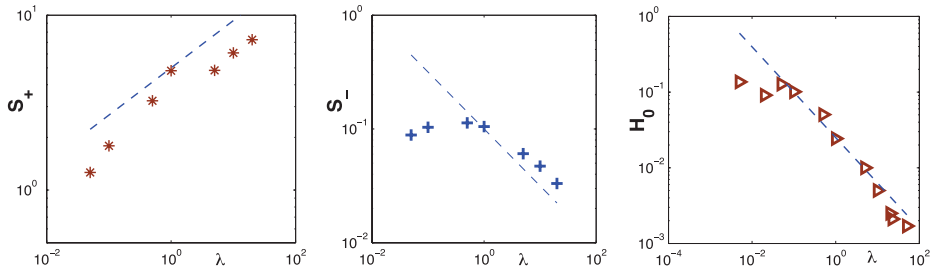

FIG. 5. The cone slope S_+ (left panel) and S_- (centre panel) together with the parameter H_0 (right panel, where $h_{\min} = H_0\tau$) versus λ. The dashed lines indicate a fit to the power laws $S_+ \sim \lambda^{0.27}$, $S_- \sim \lambda^{-0.5}$ and $H_0 \sim \lambda^{-0.6}$.

resemble the results of Zhang & Lister (1999) and Sierou & Lister (2003). In the first of these two studies, the results of time-dependent boundary integral computations of a pinching profile are given in the range $\frac{1}{16} \leqslant \lambda \leqslant 16$ while in the second study the boundary integral formulation is expressed directly in terms of similarity variables and the range is extended to $0.002 \leqslant \lambda \leqslant 500$. The data of Fig. 4 show the approach to constant profile slope as $\xi \to \pm\infty$ as noted in these two studies and in Lister & Stone (1998). This marks the connection to a pair of axisymmetric cones on either side of the pinch point, with a steeper cone of slope S_+ and a shallower cone of slope S_-.

The data show a monotone increase of S_+ and non-monotone behaviour of S_- as λ increases, and a maximum of S_- occurs when $\lambda \simeq 0.5$. The dependence of the cone slope on λ is explored further in the data of Fig. 5. There, the left panel shows S_+ versus λ in a log–log plot, which includes a dashed line of slope 0.27. This is the scaling relation for S_+ given by Sierou & Lister (2003) for large λ and is in close agreement with the experimental result of Cohen *et al.* (1999) that $S_+ \sim \lambda^{0.22\pm0.07}$ over a broad range of λ. The centre panel of Fig. 5 reiterates the non-monotone behaviour of S_-, and its dashed line has slope -0.5 to show the fit of the data to $S_- \sim \lambda^{-0.5}$ for $\lambda > 1$ which has been noted by Zhang & Lister (1999). The right panel of the figure shows H_0 versus λ, where $h_{\min} = H_0\tau$ as $\tau \to 0$; here the dashed line has slope -0.6 while the experimental data of Cohen *et al.* (1999) suggest the scaling relation $H_0 \sim \lambda^{-0.53\pm0.05}$.

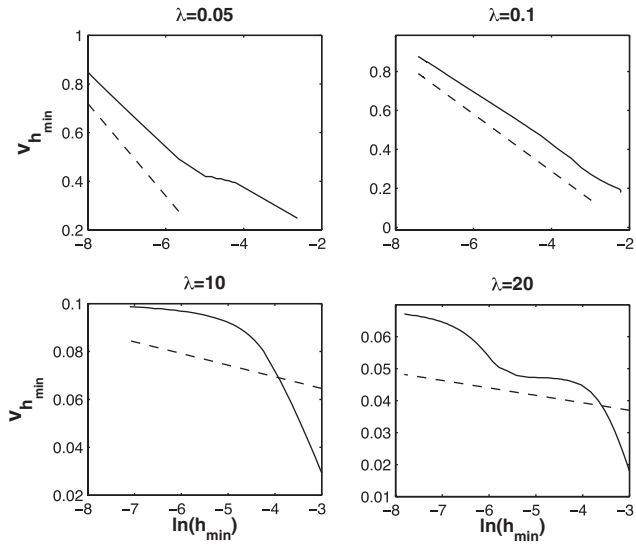

FIG. 6. Axial velocity $v_{h_{\min}}$ at the minimum thread radius $z = h_{\min}$ versus $\ln(h_{\min})$ for values of the viscosity ratio λ from 0.05 to 20, indicating logarithmic increase in axial velocity near pinch-off. Solid lines show the simulation results. Dashed lines in the top two panels for small λ ($\lambda = 0.05$ and $\lambda = 0.1$) are obtained by neglecting the contribution from the double layer potential of (4.1) and (4.3), while the dashed lines in the lower two panels for larger λ ($\lambda = 10$ and $\lambda = 20$) include the double layer contribution.

Lister & Stone (1998) give an estimate for the linear increase of the axial velocity at the minimum radius $v_{h_{\min}}$ with $\ln(h_{\min})$ when $\lambda = 1$ by analysis of the flow induced by surface tension in the asymptotic cones that neighbour the vicinity of the minimum radius or pinch point. This is given by estimating the right-hand side of (4.1) due to the single layer potential over the cone surfaces. The result can be generalized to include $\lambda \neq 1$ by estimating the integral on the left-hand side of (4.1) due to the double layer potential, and if we make the approximation that $v \gg u$ with $v \simeq$ constant on the cone surfaces, which is expected to hold for large λ, we find that the contribution to v due to a single cone with semi-angle α is

$$\left(\frac{1+\lambda}{2} + (\lambda - 1)\frac{3}{8}\sin^2 2\alpha\right) v_{h_{\min}} \sim \frac{1}{8}\sin 2\alpha \ln(h_{\min}). \tag{4.3}$$

The net contribution to v due to both cones is given by linear superposition, with cone angles α_l and α_r. In Fig. 6, the solid lines show $v_{h_{\min}}$ versus $\ln(h_{\min})$ from our computational data, with nearly linear behaviour in the final stage as $h_{\min} \to 0$ when pinch-off is approached. The dashed lines in the top two panels of the figure give the estimate for $v_{h_{\min}}$ of (4.3) for small λ when the contribution from the double layer potential, which is proportional to $\lambda - 1$, is neglected. In the lower two panels, the dashed line gives the estimate of $v_{h_{\min}}$ of (4.3) for large λ with the contribution due to the double layer potential included.

5. Conclusion

Capillary pinching of a viscous thread or drop immersed in another viscous fluid has been considered analytically and computationally at zero Reynolds numbers. The viscosity ratio between inner and outer

fluids is arbitrary. The first part of the study considers the emergence of long-wave models as the viscosity ratio λ varies. Three canonical models are found at increasingly larger values of λ, and the analysis is found in Section 2. The lowest and largest viscosity ratio models, $\lambda \sim \epsilon^2$ and $\lambda \sim 1/(\epsilon^2 \ln(1/\epsilon))$, respectively, are well-posed and provide appropriate limiting forms for the inner or outer region being air, respectively. The intermediate case $\lambda \sim 1/\ln(1/\epsilon)$ is ill-posed, however, and indicates that a long-wave model may not be appropriate in this case. This is consistent with our direct numerical simulations for arbitrary λ based on boundary integral methods that show that, at intermediate λ, a self-similar solution emerges but with unit aspect ratio. Additional investigation of the derived long-wave models and comparison with additional direct simulations is beyond the scope of the present work and is currently being studied by the authors.

Funding

The authors acknowledge support from National Science Foundation grants DMS-0708977 and DMS-1009105.

References

Acrivos, A. & Lo, T. (1978) Deformation and breakup of a single slender drop in an extensional flow. *J. Fluid Mech.*, **86**, 641–672.

Anna, S., Bontoux, N. & Stone, H. (2003) Formation of dispersions using 'flow focusing' in microchannels. *Appl. Phys. Lett.*, **82**, 364–366.

Brenner, M. P., Lister, J. R. & Stone, H. A. (1996) Pinching threads, singularities and the number 0.0304.... *Phys. Fluids*, **8**, 2827–2836.

Buckmaster, J. (1972) Pointed bubbles in slow viscous flow. *J. Fluid Mech.*, **55**, 385–400.

Chauhan, A., Maldarelli, C., Papageorgiou, D. & Rumschitzki, D. (2006) The absolute instability of an inviscid compound jet. *J. Fluid Mech.*, **549**, 81–98.

Chen, A., Notz, P. & Basaran, O. (2002) Computational and experimental analysis of pinch-off and scaling. *Phys. Rev. Lett.*, **88**, 174501–174504.

Cohen, I., Brenner, M., Eggers, J. & Nagel, S. (1999) Two fluid drop snap-off problem: experiments and theory. *Phys. Rev. Lett.*, **83**, 1147–1150.

Doshi, P., Cohen, I., Zhang, W., Siegel, M., Howell, P., Basaran, O. & Nagel, S. (2003) Persistence of memory in drop breakup: the breakdown of universality. *Science*, **302**, 1185–1188.

Eggers, J. & Dupont, T. (1994) Drop formation in a one-dimensional approximation of the Navier–Stokes equation. *J. Fluid Mech.*, **262**, 205–221.

Fokas, A. & Papageorgiou, D. (2005) Absolute and convective instability for evolution PDEs on the half-line. *Stud. Appl. Math.*, **114**, 95–114.

Geer, J. & Keller, J. (1968) Uniform asymptotic solutions for potential flow around a thin airfoil and the electrostatic potential about a thin conductor. *SIAM J. Appl. Math.*, **16**, 75–101.

Hameed, M., Siegel, M., Young, Y.-N., Li, J., Booty, M. & Papageorgiou, D. (2008a) Influence of insoluble surfactant on the deformation and breakup of a bubble or thread in a viscous fluid. *J. Fluid Mech.*, **594**, 307–340.

Hameed, M., Siegel, M., Young, Y. N., Li, J., Booty, M. R. & Papageorgiou, D. T. (2008b) Influence of insoluble surfactant on the deformation and breakup of a bubble or thread in a viscous fluid. *J. Fluid Mech.*, **594**, 307–340.

Handelsman, R. & Keller, J. (1967) Axially symmetric potential flow around a slender body. *J. Fluid Mech.*, **28**, 131–147.

Hyman, J. & Nicolaenko, B. (1986) The Kuramoto–Sivashinsky equation: a bridge between PDEs and dynamical systems. *Phys. D*, **18**, 113–126.

Keller, J., Rubinow, S. & Tu, Y. (1973) Spatial instability of a jet. *Phys. Fluids*, **16**, 2052–2055.

Kowalewski, T. (1996) On the separation of droplets from a liquid jet. *Fluid Dyn. Res.*, **17**, 121–145.
Lister, J. & Stone, H. (1998) Capillary breakup of a viscous thread surrounded by another viscous fluid. *Phys. Fluids*, **10**, 2758–2764.
Newhouse, L. & Pozrikidis, C. (1992) The capillary instability of annular layers and liquid threads. *J. Fluid Mech.*, **242**, 193–209.
Papageorgiou, D. (1995) On the breakup of viscous liquid threads. *Phys. Fluids*, **7**, 1529–1544.
Pozrikidis, C. (1999) Capillary instability and breakup of a viscous thread. *J. Eng. Math.*, **36**, 255–275.
Rayleigh, L. (1892) On the instability of cylindrical fluid surfaces. *Philos. Mag.*, **34**, 177–180.
Sierou, A. & Lister, J. (2003) Self-similar solutions for viscous capillary pinch-off. *J. Fluid Mech.*, **497**, 381–403.
Wang, Q. & Papageorgiou, D. (2011) Dynamics of a viscous thread surrounded by another viscous fluid in a cylindrical tube under the action of a radial electric field: breakup and touchdown singularities. *J. Fluid Mech.*, **683**, 27–56.
Zhang, W. & Lister, J. (1999) Similarity solutions for capillary pinch-off in fluids of differing viscosity. *Phys. Rev. Lett.*, **83**, 1151–1154.

Appendix

For the scaling $\lambda \sim \epsilon^2$ at item 1 of Section 2.3.1, set

$$\lambda = \lambda_0 \epsilon^2, \quad f = \epsilon f_0 + \cdots, \quad g = \epsilon g_0 + \cdots, \quad \delta = 1, \tag{A.1a}$$

$$u_z = (1/\epsilon) u_{z0} + \cdots, \quad u_r = u_{r0} + \cdots, \quad p = p_0 + \cdots, \quad \tilde{R} = R_0 + \cdots. \tag{A.1b}$$

This scaling retains all terms among (2.21), and hence all leading terms among the components of the stress-balance boundary conditions (2.18) and (2.19), which become

$$\frac{\partial p_0}{\partial z}\frac{R_0}{4} = -\frac{2f_0}{R_0} - \frac{2g_0 R_0'}{R_0^2} + \frac{2g_0'}{R_0}, \quad \text{tangential stress balance,} \tag{A.2}$$

$$p_0 - \frac{4g_0}{R_0^2} = \frac{1}{R_0}, \quad \text{normal stress balance.} \tag{A.3}$$

In this scaling regime, the continuity of velocity and the kinematic condition as expressed by (2.26–2.28) are modified by setting the Stokeslet distribution f_0 to zero. When this is done, after eliminating B_0 between the relations analogous to (2.26) and (2.27), one finds an expression for g_0. Using this to eliminate g_0 in the relation analogous to (2.28), the result (on dropping subscripts) is (2.23). When the expression for g_0 is substituted in (A.3), one finds (on dropping subscripts) (2.24).

The Stokeslet strength f_0 uncouples from the leading-order dynamics in this scaling regime, as noted in Hameed *et al.* (2008a). It can be found from (A.2).